

# Heterobilayer Ferroelectricity with Competitive Polarization

Xian Wang, Jun Zhou, Xuesen Wang, Lei Shen,\* and Yuan Ping Feng\*



Cite This: <https://doi.org/10.1021/acsnano.5c11217>



Read Online

ACCESS |

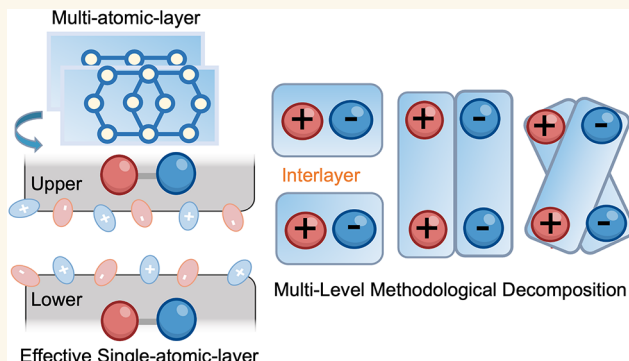
Metrics & More

Article Recommendations

Supporting Information

**ABSTRACT:** Two-dimensional ferroelectrics with large out-of-plane polarization (OOP) are promising for the design of low-power memory and logic devices, but their experimental realization remains limited due to the scarcity of homobilayers and the complexity of heterobilayers. Here, we perform high-throughput screening of 24,960 configurations and identify 43 semiconducting heterobilayer ferroelectrics with an OOP exceeding the experimentally reported value in MoS<sub>2</sub>/WS<sub>2</sub> while maintaining sliding barriers below 100 meV/f.u. Among them, CdO/InN exhibits an OOP nearly 50 times greater than that of MoS<sub>2</sub>/WS<sub>2</sub>, along with a low sliding barrier of around 35 meV/f.u., making it a candidate that combines strong polarization with low-energy switching. The data analysis shows that heterobilayers composed of single-atom-layer monolayers mostly exhibit enhanced sliding ferroelectric behavior, providing a library of ferroelectrics. In addition, we develop a multiscale physical model that links monolayer characteristics to the sliding ferroelectric response by combining structural projection and polarization decomposition. This physical mechanism reveals a crucial competition between interlayer and intralayer dipoles in heterobilayer systems.

**KEYWORDS:** high-throughput calculation, two-dimensional ferroelectrics, heterobilayers, vertical polarizations, decomposed dipole contributions



## INTRODUCTION

Ferroelectrics (FEs) enable critical technologies from non-volatile memories to sensors,<sup>1–5</sup> yet conventional systems remain limited by either in-plane polarization (IPP) or disruptive ion-displacement mechanisms.<sup>6,7</sup> Out-of-plane polarization (OOP) emerges as a superior alternative, offering suppressed quantum tunneling and enhanced nanoscale performance essential for next-generation devices.<sup>8,9</sup> The search for low-power and switchable OOP FEs has thus shifted attention toward two-dimensional (2D) materials, which offer structural flexibility, reduced dimensionality, and weak interlayer van der Waals (vdW) interactions.<sup>10–12</sup> While substantial progress has been made in identifying IPP FEs in 2D monolayers, OOP remains rare.<sup>13–16</sup> A high-throughput screening of 252 monolayers in the C2DB database by Kruse et al.<sup>14</sup> revealed 49 IPP FEs, but only eight with intrinsic OOP and six exhibiting coupled IPP/OOP behavior. Wu et al.<sup>15</sup> screened the 2DMatPedia database<sup>17</sup> and identified more monolayer OOP FEs, but most have very low polarization. This scarcity is largely attributed to the limited availability of polar space groups among known bulk crystal structures, which restricts spontaneous symmetry breaking in monolayer systems. Bilayer structures, however, offer additional opportunities for

symmetry engineering. Particularly, breaking inversion symmetry through tailored stacking arrangements, such as interlayer sliding or twisting, can induce OOP that is both switchable and tunable.<sup>18–21</sup> The weak vdW interactions between layers reduce the energy cost of such structural transitions, enabling reversible polarization at lower energy barriers.<sup>22,23</sup>

Despite growing interest, research to date has largely focused on *homobilayer* systems, which are inherently constrained by the limited pool of 2D monolayers and often exhibit high structural symmetry that restricts the emergence of diverse polarization states.<sup>24–29</sup> For example, Wang et al.<sup>29</sup> started from 79 monolayer semiconductors with honeycomb structures, leading to the construction of 79 homobilayers. In contrast, vdW *heterobilayers*, formed by stacking two distinct monolayers, unlock a vastly richer design space, offering a broad spectrum of interfacial chemistries, broken symmetries, and tunable

Received: July 4, 2025

Revised: August 26, 2025

Accepted: August 26, 2025

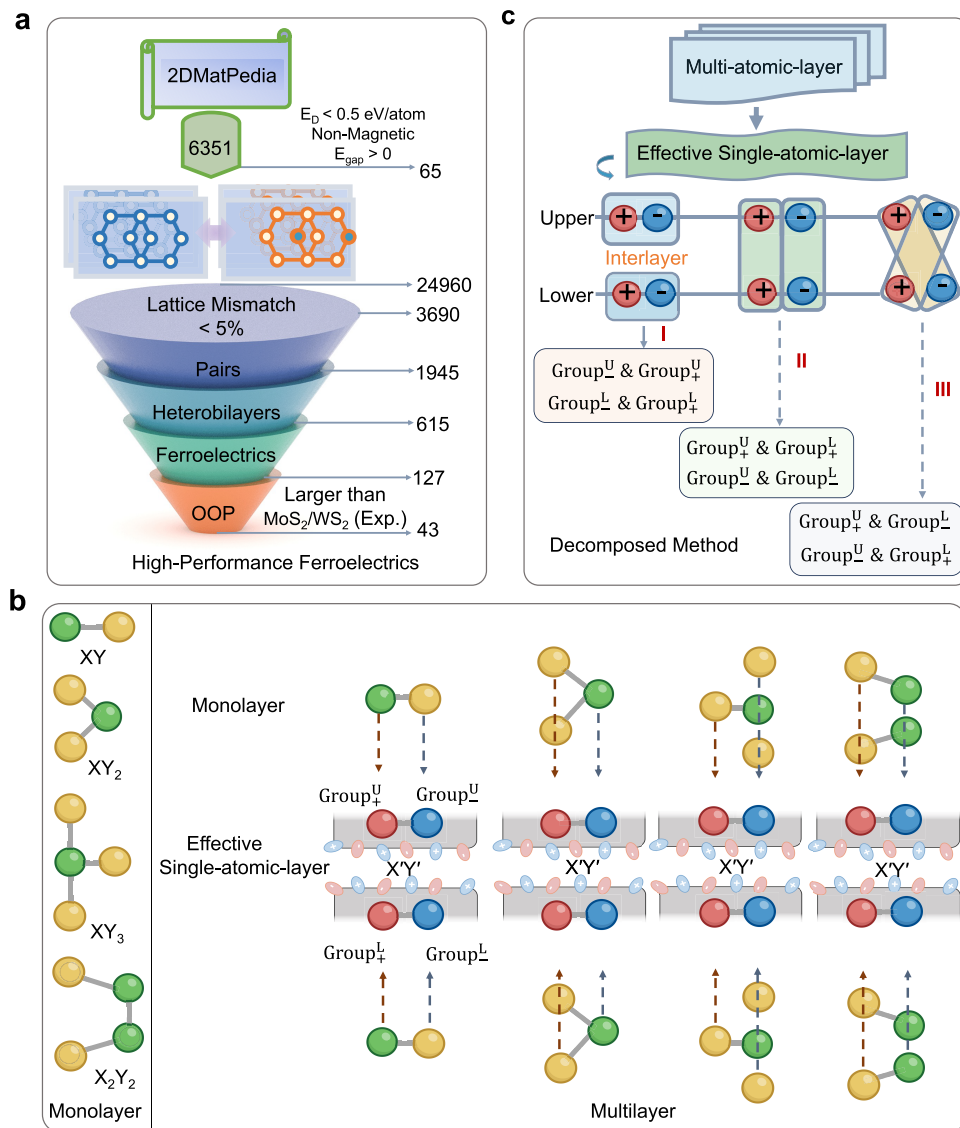


**Figure 1.** Overview of the screening framework and decomposed polarization method. (a) Workflow for identifying semiconducting candidates with strong OOP and low sliding energy barriers. (b) Schematic of monolayer characteristics and the projection scheme linking multiatomic-layer configurations to their single-atomic-layer counterparts. (c) Illustration of the dipole decomposition framework, which resolves total OOP into localized and delocalized contributions across intra-atomic, interatomic, atomic group, and layer-specific levels.

electronic environments.<sup>30–34</sup> For example, the 79 monolayer honeycomb materials can construct 6162 heterobilayers and 36,972 sliding structures. This expanded configurational landscape holds immense potential for discovering heterobilayers with enhanced OOP, alternative switching mechanisms, and multifunctional properties.

Due to the complexity of interfacial interactions in heterostructures, the *ferroelectric mechanism* is much more complex in homostructures. In homobilayer structures, the same atomic pairs exist both within and out of the plane. For instance, only B–N, B–B, and N–N pairs are present in bilayer h-BN (both in and across the layers), and the mirror symmetry results in identical polarization on both sides. On the other hand, heterobilayers such as MoS<sub>2</sub>/WTe<sub>2</sub> have a variety of possible atomic pairings, including Mo–S, W–Te, Mo–W, Mo–Te, W–S, and W–Mo, leading to different polarization on either side. More importantly, the mere presence of OOP does not guarantee ferroelectric switchability, and many heterobilayers fail to satisfy the essential criteria for practical sliding

ferroelectrics, posing a substantial obstacle to experimental realization and device integration.<sup>35</sup> A landmark study by Rogee et al.<sup>36</sup> provided the experimental demonstration of switchable FE in MoS<sub>2</sub>/WS<sub>2</sub> heterobilayers by sliding, highlighting the feasibility of the sliding FE in heterobilayer materials. Nevertheless, the observed OOP remains small (<1 pC/m), and general design principles for identifying and optimizing high-performance sliding FEs in heterobilayers are still lacking. Moreover, the governing mechanism of heterobilayer ferroelectricity is not clear.

To address these critical gaps, we developed a high-throughput computational framework for the discovery and design of sliding FEs in 2D vdW heterobilayers. By screening tens of thousands of heterostructures constructed from hexagonal monolayers in the 2DMatPedia database,<sup>17</sup> we identify a diverse set of previously unexplored candidates exhibiting robust and switchable OOP. Descriptor analysis reveals that the emergence and strength of OOP are governed by several key factors, including electronegativity difference,

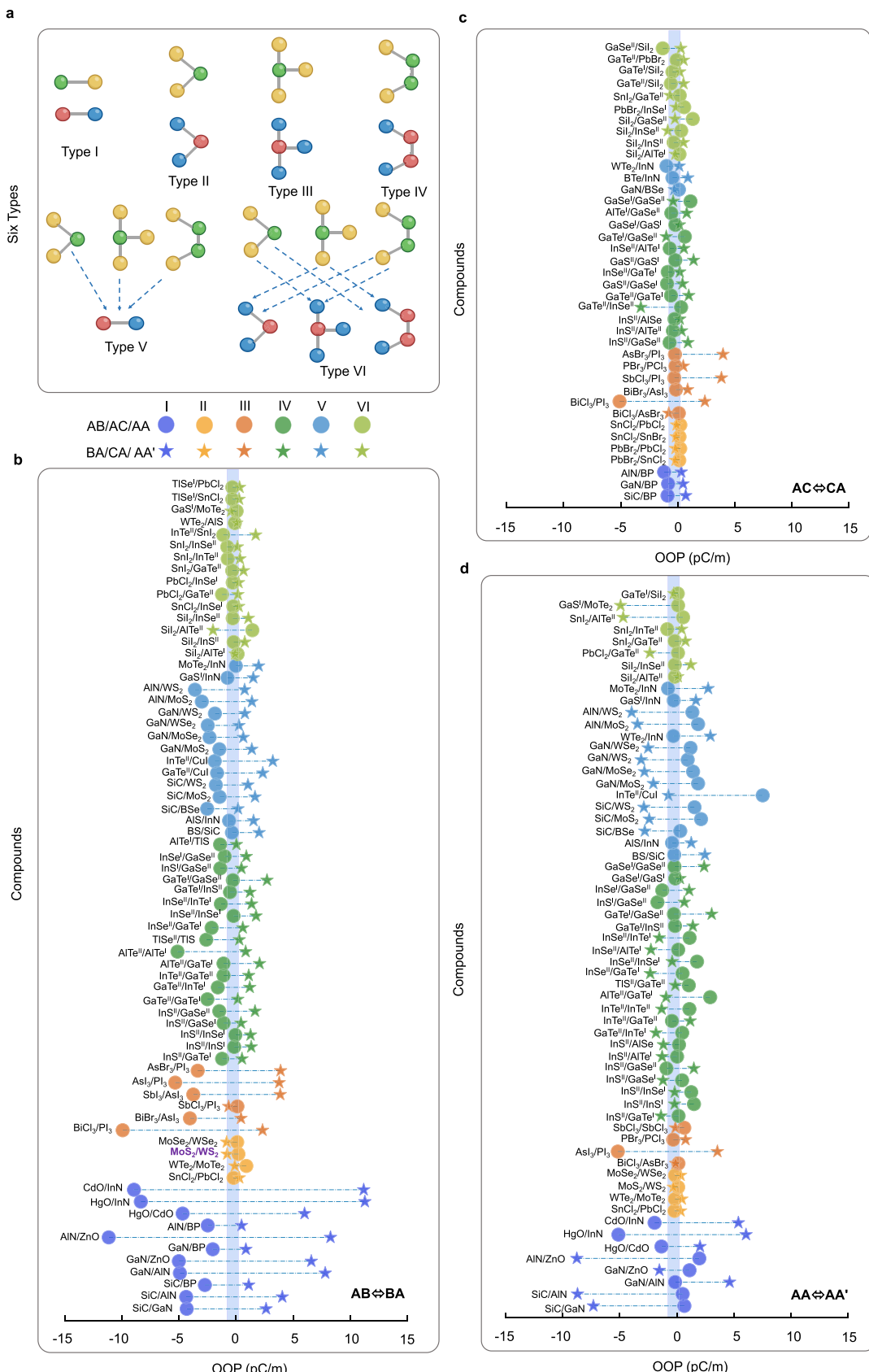


**Figure 2.** Stacking-dependent ferroelectricity in 2D heterobilayers. (a) Classification of heterobilayer materials into six stacking types based on the atomic-layer composition of the upper and lower monolayers, which can be either single-atomic-layer or multilayer structures. OOP values for (b) AB/BA and (c) AC/CA stackings, demonstrating sliding ferroelectric responses induced by in-plane displacement between layers, leading to polarization emergence and reversal. (d) OOP values for AA and AA' stackings reveal polarization reversal driven by in-plane 180° twisting. The shaded light-blue background indicates the experimentally realized MoS<sub>2</sub>/WS<sub>2</sub> used as a reference.

interfacial charge transfer, stacking geometry, interlayer spacing, and van der Waals radius. They offer quantitative design guidelines for stabilizing the FE in 2D heterostructures. To complement these insights, we establish a physical picture linking monolayer structural features to OOP, providing a deeper understanding of the sliding ferroelectric mechanism and its compositional dependence. To bridge structure–property relationships across scales, we construct a projection scheme connecting multiautomatic-layer configurations to their equivalent single-atomic-layer constituents. A polarization decomposition method further resolves total polarization into localized and delocalized components, enabling a direct correlation between monolayer properties and ferroelectric behavior. This approach enables a fine-grained spatial resolution of OOP contributions at the intra-atomic, interatomic, atomic group, and layer-specific levels, revealing subtle polarization mechanisms that are otherwise obscured within the compressed vertical dimension of 2D materials. The competition between interlayer- and intralayer-driven polarization emerges as a key factor governing the overall ferroelectric response, with single-atom-layer monolayers frequently forming heterostructures that exhibit particularly favorable sliding behavior. Altogether, our integrated framework not only accelerates the discovery of high-performance ferroelectric materials but also provides a generalizable strategy for interpreting and engineering their fundamental mechanisms. This offers predictive design rules for next-generation low-power ferroelectric and multifunctional vdW devices.

## RESULTS AND DISCUSSION

**Heterobilayer Design Based on 2DMatPedia.** The overall high-throughput computation workflow is illustrated in Figure 1a. From the 2DMatPedia database comprising over 6000 2D materials, 65 hexagonal monolayers are selected in terms of nonmagnetism, layer group No. 78, decomposition energies below 0.5 eV/atom, and nonzero band gaps.<sup>17,37</sup> All monolayer structures were systematically constructed either via exfoliation from layered bulk structures (top-down approach) or through chemical substitution from known monolayers lacking layered bulk counterparts (bottom-up approach).<sup>17</sup> Using these monolayers, bilayer heterostructures of the form  $X_L Y_L / X_U Y_U$ , where  $X_L Y_L$  and  $X_U Y_U$  denote, respectively, the lower (L) and upper (U) layers, were constructed through lattice rotation and translation, with lattice mismatch constrained below 5%. This process yielded approximately 3,690 stacking configurations. Six primary stacking patterns are identified: AA, AA', AB, BA, AC, and CA, with detailed descriptions provided in Figure S1. Based on the distinct characteristics of sliding and twisting FE, these stacking patterns are classified into three categories: AA(AA'), AB(BA), and AC(CA). The selected monolayer materials exhibit both single-atomic-layer and multiautomatic-layer characteristics, as shown in Figure 1b. Throughout the discussion, the six stacking patterns refer to AA(AA'), AB(BA), and AC(CA), while the six stacking types correspond to the identified types I–VI, respectively; see Figure 2a.

**Out-of-Plane Polarization of Heterobilayer Materials.** AB and BA stackings are the most frequently observed configurations in sliding FEs,<sup>18,19,24</sup> with their predicted OOP values shown in Figure 2b and Table S1 in the Supporting Information (SI). We use the experimentally reported MoS<sub>2</sub>/WS<sub>2</sub> heterobilayer as a benchmark system.<sup>36</sup> The MoS<sub>2</sub>/WS<sub>2</sub> heterobilayer adopts the same stacking configuration as that reported in the experimental work.<sup>36</sup> The calculated OOP values

are 0.21 pC/m for AB and −0.78 pC/m for BA, in good agreement with experimental values of approximately 0.10 and −1.00 pC/m, respectively.<sup>36</sup> In particular, 60 heterobilayers exhibit bidirectional OOP values that exceed those of MoS<sub>2</sub>/WS<sub>2</sub>. A systematic comparison across the six stacking types shows that type I exhibits the largest OOP, followed by type III; types IV and V show moderate values, while types II and VI exhibit the weakest. Among semiconducting bilayers, CdO/InN exhibits the strongest OOP, up to 50 times and 5 times higher than that of heterobilayer MoS<sub>2</sub>/WS<sub>2</sub><sup>36</sup> and homobilayer h-BN,<sup>19</sup> respectively. While HgO/InN shows an even larger OOP, its metallic nature excludes it from the semiconducting candidates, making CdO/InN the top-performing semiconducting heterobilayer in our study.

For type I, the 11 heterobilayers exhibit significantly higher OOP compared to MoS<sub>2</sub>/WS<sub>2</sub>. Notable examples include CdO/InN (−8.94, 11.18 pC/m) and AlN/ZnO (−11.15, 8.27 pC/m). For type II, the OOP values are generally small, with SnCl<sub>2</sub>/PCl<sub>2</sub> achieving −0.22 and 0.28 pC/m and MoSe<sub>2</sub>/WSe<sub>2</sub> reaching 0.10 and −0.82 pC/m, with a direction exceeding those of MoS<sub>2</sub>/WS<sub>2</sub>. In type III, five heterobilayers exhibit high OOP values. Leading examples include BiCl<sub>3</sub>/PI<sub>3</sub> (−9.93 and 2.32 pC/m), followed by AsI<sub>3</sub>/PI<sub>3</sub> (−5.33 and 3.78 pC/m) and AsBr<sub>3</sub>/PI<sub>3</sub> (−3.36 and 3.90 pC/m). For type IV, the OOP values are generally moderate, mostly below 2 pC/m. Notable exceptions include AlTe<sup>II</sup>/AlTe<sup>I</sup>, which achieves the highest OOP values at −5.13 and 0.84 pC/m. Several heterobilayers, such as InS<sup>II</sup>/GaSe<sup>II</sup> and GaTe<sup>II</sup>/InTe<sup>I</sup>, exhibit bidirectional values exceeding 1 pC/m. For type V, the maximum OOP reaches 3.6 pC/m, with notable examples including SiC/MoS<sub>2</sub> and InTe<sup>II</sup>/Cu<sup>I</sup>. In contrast, type VI generally exhibits small values of the OOP, mostly below 1 pC/m, with the highest values observed in SiI<sub>2</sub>/AlTe<sup>II</sup> and InTe<sup>II</sup>/SnI<sub>2</sub>.

Although previous theoretical and experimental studies have shown that AC and CA stackings in homobilayers yield zero OOP,<sup>18,24,29</sup> our study demonstrates that sliding FEs also emerge in AC and CA stacking patterns, as shown in Figure 2c and Table S2. Such behavior is predominantly observed in heterobilayers composed of multiautomatic-layer monolayers. Although the overall OOP in AC and CA configurations is generally modest, 24 systems exhibit values exceeding those of MoS<sub>2</sub>/WS<sub>2</sub>. Representative examples include BiCl<sub>3</sub>/PI<sub>3</sub> (−5.1, 2.37 pC/m), AsBr<sub>3</sub>/PI<sub>3</sub> (−0.25, 3.96 pC/m), SbCl<sub>3</sub>/PI<sub>3</sub> (−0.31, 3.82 pC/m), and GaTe<sup>II</sup>/InSe<sup>II</sup> (−0.29, −3.20 pC/m). This not only broadens the understanding of stacking-dependent ferroelectricity but also reveals the potential of AC and CA stackings in the design of unconventional ferroelectric devices.

Beyond sliding-induced OOP in AB(BA) and AC(CA) stackings, we show that in-plane 180° twisting between AA and AA' configurations can also drive polarization reversal in heterobilayers, as illustrated in Figure 2d and Table S3. Despite the theoretical prediction of zero OOP in AA and AA' configurations of homobilayers, significant OOP values are observed in their heterostructured counterparts.<sup>18,24,29</sup> In total, 41 heterobilayers exhibit bidirectional OOP values surpassing those of MoS<sub>2</sub>/WS<sub>2</sub>. Among the six stacking types, type I yields the widest OOP range (0.3–8.76 pC/m), with notable examples including AlN/ZnO, SiC/AlN, SiC/GaN, and HgO/InN. Type III follows with a moderate range (0.11–5.17 pC/m), exemplified by AsI<sub>3</sub>/PI<sub>3</sub>, while type V spans 0.06–3.96 pC/m, including AlN/MoS<sub>2</sub>, GaN/MoS<sub>2</sub>, and SiC/MoS<sub>2</sub>. In contrast, types II, IV, and VI generally exhibit smaller OOP values (<1

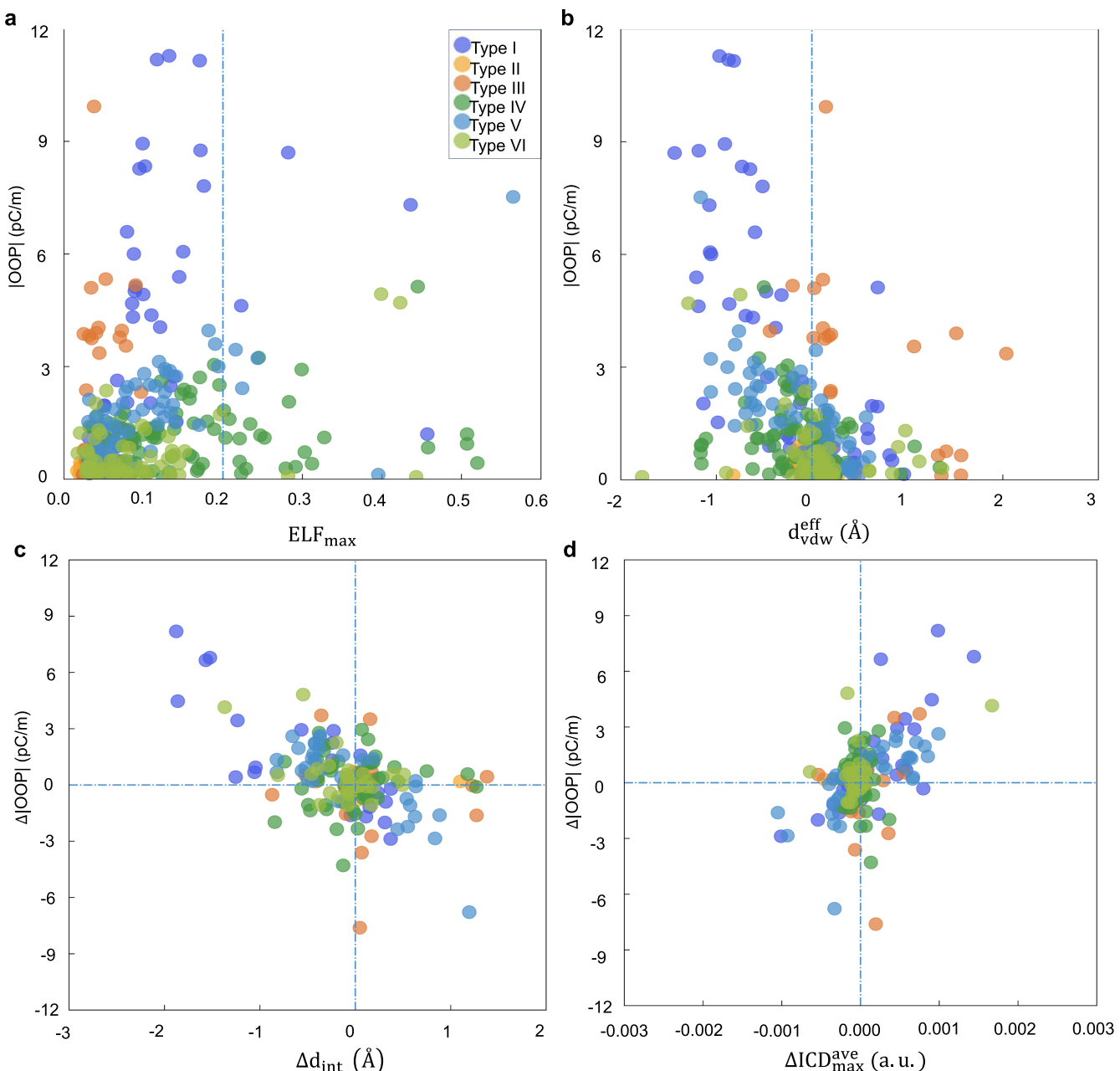


**Figure 3.** Correlating the OOP with interfacial electronic and structural descriptors. (a) The strength of the OOP versus the interlayer maximum electron localization function ( $\text{ELF}_{\max}$ ) and (b) effective vdW radius interlayer distance ( $d_{\text{vdw}}^{\text{eff}}$ ). (c) The relationship between the change in absolute OOP ( $\Delta|\text{OOP}|$ ) and the change in the interlayer distance ( $\Delta d_{\text{int}}$ ), and (d) the change of the maximum ion charge difference ( $\Delta \text{ICD}_{\max}^{\text{ave}}$ ) between monolayer and corresponding bilayer.

pC/m), with exceptions such as InTe<sup>II</sup>/CuI and AlTe<sup>II</sup>/GaTe<sup>I</sup>. These results demonstrate that in-plane twisting offers a complementary route to interlayer sliding for realizing a reversible FE in diverse stacking configurations.

A total of 127 distinct heterobilayers are found to exhibit sliding- or twisting-induced FE. Among them, seven heterobilayers exhibited OOP switching across all six stacking configurations, indicating robust sliding and twisting ferroelectric behavior. These include SiI<sub>2</sub>/AlTe<sup>II</sup>, SiI<sub>2</sub>/InSe<sup>II</sup>, SnI<sub>2</sub>/GaTe<sup>II</sup>, InS<sup>II</sup>/GaSe<sup>II</sup>, InSe<sup>II</sup>/GaTe<sup>I</sup>, GaN/WSe<sub>2</sub>, and GaTe<sup>I</sup>/GaSe<sup>II</sup>. These findings suggest a general design principle: heterobilayers constructed from monolayers with single-atom-layer structures tend to display strong OOP. Among all stacking types, AB and BA configurations are most likely to support

sliding FE with a high-polarization strength. Overall, our results demonstrate that both interlayer sliding and in-plane twisting are effective routes to induce and control switchable polarization in 2D heterostructures.

**Factors Influencing Out-of-Plane Polarization.** The strength of OOP is generally characterized by multiple factors,<sup>18,24,29,38</sup> including the electron localization function (ELF), effective vdW interlayer distance  $d_{\text{vdw}}^{\text{eff}}$  (see Figure S2 for a detailed definition), interlayer distance ( $d_{\text{int}}$ ), ion charge difference (ICD) between monolayer and bilayer configurations, and elemental electronegativity (E). The maximum ELF ( $\text{ELF}_{\max}$ ) is defined as the maximum ELF value located in the midregion between the lowest atoms of the upper layer and the highest atoms of the lower layer. As depicted in Figure 3a, most

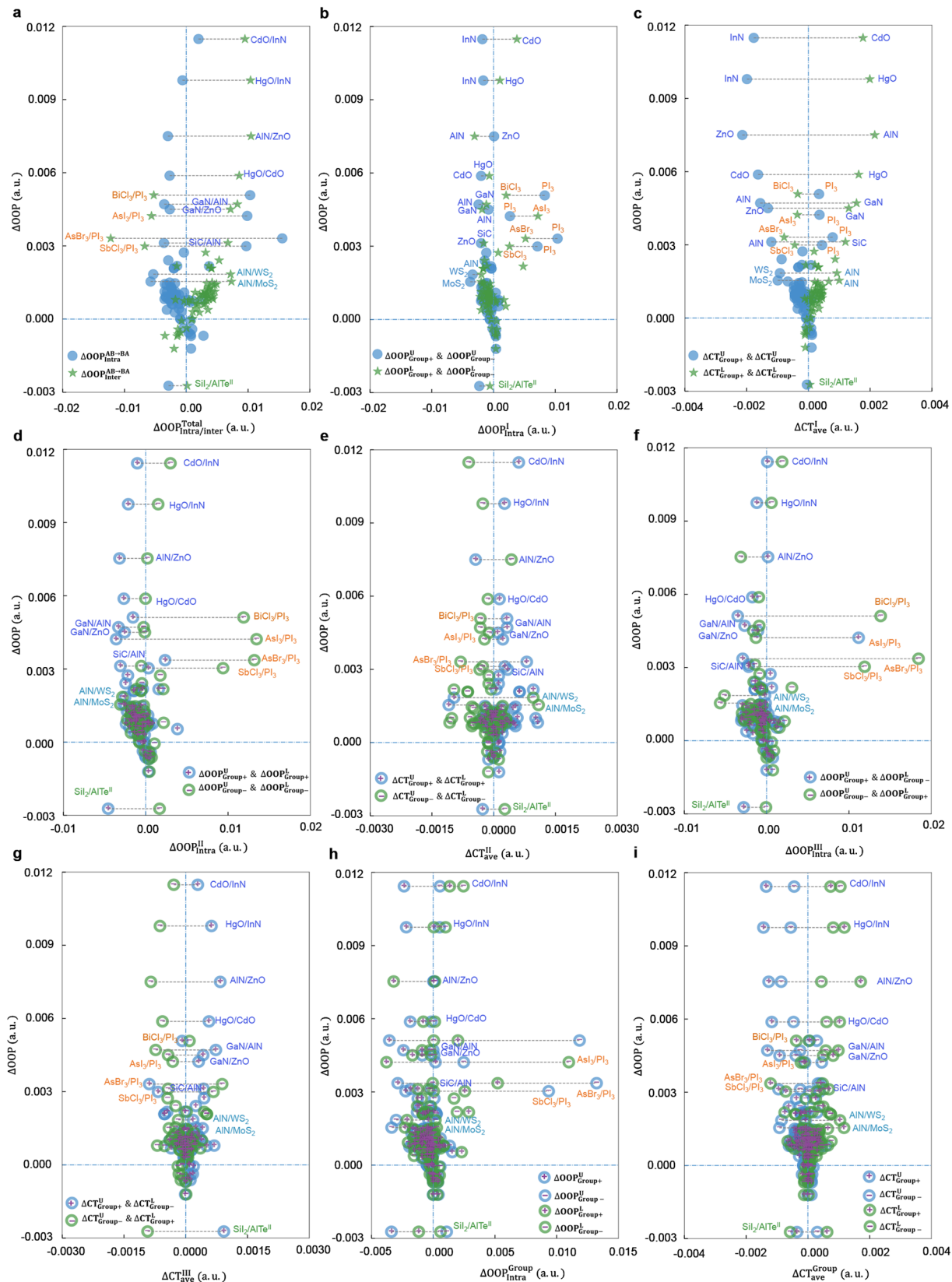


**Figure 4. Multilevel decomposition of sliding-induced OOP into local and nonlocal contributions.** (a) The change in the level of the OOP is decomposed into intra- and interlayer contributions during the sliding process. The intralayer (b) and interlayer (c) contributions are further attributed to individual layers. The localized and nonlocal charge-transfer contributions positive–positive (d, e), and cross positive–negative groups (f, g) between the upper and lower layers. (h) The localized and (i) nonlocal charge-transfer contributions in positive (Group+) and negative (Group-) atomic groups within the upper and lower layers. The highlighted bright blue, orange, sky blue, and light green fonts represent type I, type III, type V, and type VI, respectively.

studied heterobilayers exhibit low values for  $\text{ELF}_{\max}$  (less than 0.2), indicating weak vdW interlayer interactions. However, a subset of materials in type IV and type VI shows  $\text{ELF}_{\max}$  values exceeding 0.3, suggesting stronger interlayer interactions. Even in most systems with high OOP, the  $\text{ELF}_{\max}$  values remain low, which is beneficial for both sliding and twisting FE. Generally, a larger  $d_{\text{vdW}}^{\text{eff}}$  value indicates weaker vdW interactions. As shown in Figure 3b, the high OOP values are often associated with negative  $d_{\text{vdW}}^{\text{eff}}$ . This trend is particularly pronounced in type I and type V materials. Interestingly, type III materials exhibit relatively high OOP values despite having large and positive  $d_{\text{vdW}}^{\text{eff}}$  values, suggesting that the strong OOP in these systems arises from mechanisms beyond just interlayer interactions.

Furthermore, we compute the variation in the interlayer distance ( $\Delta d_{\text{int}}$ ), average maximum ionic net charge ( $\Delta \text{ICD}_{\text{ave}}^{\max}$ ), and relative electronegativity difference ( $\Delta E_r$ ) between the outermost atomic species in the upper and lower layers across corresponding stacking pairs during sliding or twisting. As illustrated in Figures 3c,d and S3,  $\Delta d_{\text{int}}$  exhibits a negative correlation with OOP and a positive correlation with  $\Delta \text{ICD}_{\text{ave}}^{\max}$  in most studied structures, particularly within type I and type V systems. However, this relationship does not hold in type II, III, IV, or VI, suggesting a variation in the underlying interfacial mechanisms. For heterostructures in which the interfacial atomic species remain identical before and after sliding or twisting,  $\Delta E_r$  is zero—especially prevalent in types III, IV, and VI materials. Interestingly, despite the unchanged electronegativity contrast, these systems still exhibit substantial differences in the level of the OOP. This observation underscores the complex physical origin of the OOP, governed by the intricate interplay between the monolayer-intrinsic structure and interlayer stacking geometry in 2D heterobilayers.

While identified factors show strong correlations with OOP in homobilayers,<sup>24,29</sup> the heterobilayers exhibit more complex and distinct OOP characteristics. The asymmetric and compositionally diverse nature of heterostructures further enriches the polarization space, resulting in mechanisms fundamentally different from those in homobilayers. To investigate this complexity and enable predictive control, we develop a quantitative physical model described in the next section. This framework captures the key factors governing OOP in heterobilayers.

**Projected Structural Scheme and Polarization Decomposition Analysis.** Despite often being considered negligible, the finite thickness of 2D materials encodes critical structural and electronic information along the out-of-plane direction, which provides critical physical insights, ultimately limiting the effectiveness of material design and property optimization. To elucidate the mechanisms governing OOP in layered 2D materials, especially those within the layers, we develop a methodology to decompose the total polarization into localized and nonlocalized contributions, allowing for a clear distinction between individual intra- and interatomic, atomic group, and layer-level dipole contributions. A schematic representation of this approach is shown in Figure 1b. The total dipole moment in the out-of-plane direction ( $\mu_z$ ) of a system is defined as

$$\mu_z = \int r_z \rho(\mathbf{r}) d^3\mathbf{r} \quad (1)$$

where  $r_z$  represents the atomic position along the  $z$ -direction, and  $\rho(\mathbf{r})$  denotes the electron density at the position  $\mathbf{r}$ . OOP of the system is calculated by dividing the  $\mu_z$  by the in-plane area of the 2D material. Due to the additive nature of the dipole

moment, for a multilayer system containing  $N^A$  individual atoms or  $N^G$  atomic groups, the dipole moment can be decomposed in different ways. Based on individual atoms, the total dipole moment can be expressed as

$$\mu_z = \sum_{a=1}^{N^A} \mu_{a,z} + \sum_{a=1}^{N^A} q_a r_{a,z} \quad (2)$$

where  $\mu_{a,z}$  and  $q_a$  represent, respectively, the individual atomic dipole component along the  $z$ -direction and net charge of atom  $a \in \{1, 2, \dots, N^A\}$ , which can be evaluated using the Hirshfeld population analysis,<sup>39</sup> and  $r_{a,z}$  denotes the Cartesian coordinate. The two terms on the right side of eq 2 represent the individual atomic dipole moment and the interatomic charge-transfer contributions, respectively. Based on eq 2, its individual interatomic (OOP<sub>inter</sub><sup>atom</sup>) and intra-atomic (OOP<sub>intra</sub><sup>atom</sup>) components are further analyzed, as illustrated in Figure S4. However, an atomistic view alone is insufficient to fully capture the origin of the OOP in multilayer systems. Thus, we provide a complementary perspective that is essential for elucidating the microscopic origin of the OOP in 2D heterobilayers. For atomic groups composed of  $N^G$  units, their contributions can be decomposed into local and nonlocal components

$$\mu_z = \sum_{g=1}^{N^G} \mu_{g,z}^{\text{local}} + \sum_{g=1}^{N^G} \mu_{g,z}^{\text{non-local}} \quad (3)$$

where  $\mu_{g,z}^{\text{local}}$  denotes the local contribution of an individual atomic group  $g \in \{1, 2, \dots, N^G\}$ , calculated by

$$\mu_{g,z}^{\text{local}} = \sum_{a \in g} [\mu_{a,z} + q_a(r_{a,z} - R_{g,z})] \quad (4)$$

with  $R_{g,z}$  representing the geometric center of the atomic group  $g$ ; and the nonlocal contribution  $\mu_{g,z}^{\text{non-local}}$  can be calculated as

$$\mu_{g,z}^{\text{non-local}} = R_{g,z} \sum_{a \in g} q_a \quad (5)$$

The local part captures the contribution within individual atomic groups, while the nonlocal part contributes to the differences between atomic groups. Through the decomposition of the atomic groups, the atomic positions of all systems are projected onto the same  $xy$  plane, which simplify all atomic groups to be located only at three characteristic fractional sites:  $(1/3, 2/3, z)$ ,  $(2/3, 1/3, z)$ , and  $(0, 0, z)$ . Therefore, a direct and comprehensive comparison between single- and multiautomatic-layer systems can be constructed. Taking our binary monolayer system as an example, we projected atoms corresponding to these coordinates onto these positions in the  $xy$  plane, as shown in Figure 1b. In single-atomic-layer systems, each projection site corresponds to an individual atom, whereas in multiautomatic-layer systems, each projection site represents an individual atomic group. Since our systems are binary, this projection generates two groups: one positively charged (Group<sup>+</sup>) and another negatively charged (Group<sup>-</sup>); see Figure 1c.

In the following, the stacking configurations AB and BA are used to show further analysis of sliding FE based on the proposed atomic group decomposition. Since sliding FE in heterostructures involves two states, the investigation primarily examines the relationship between the variation of the OOP during sliding and the contributions from different components. Based on eqs (3–5) and as depicted in Figure 4a, the total OOP is decomposed into intralayer and interlayer contributions,

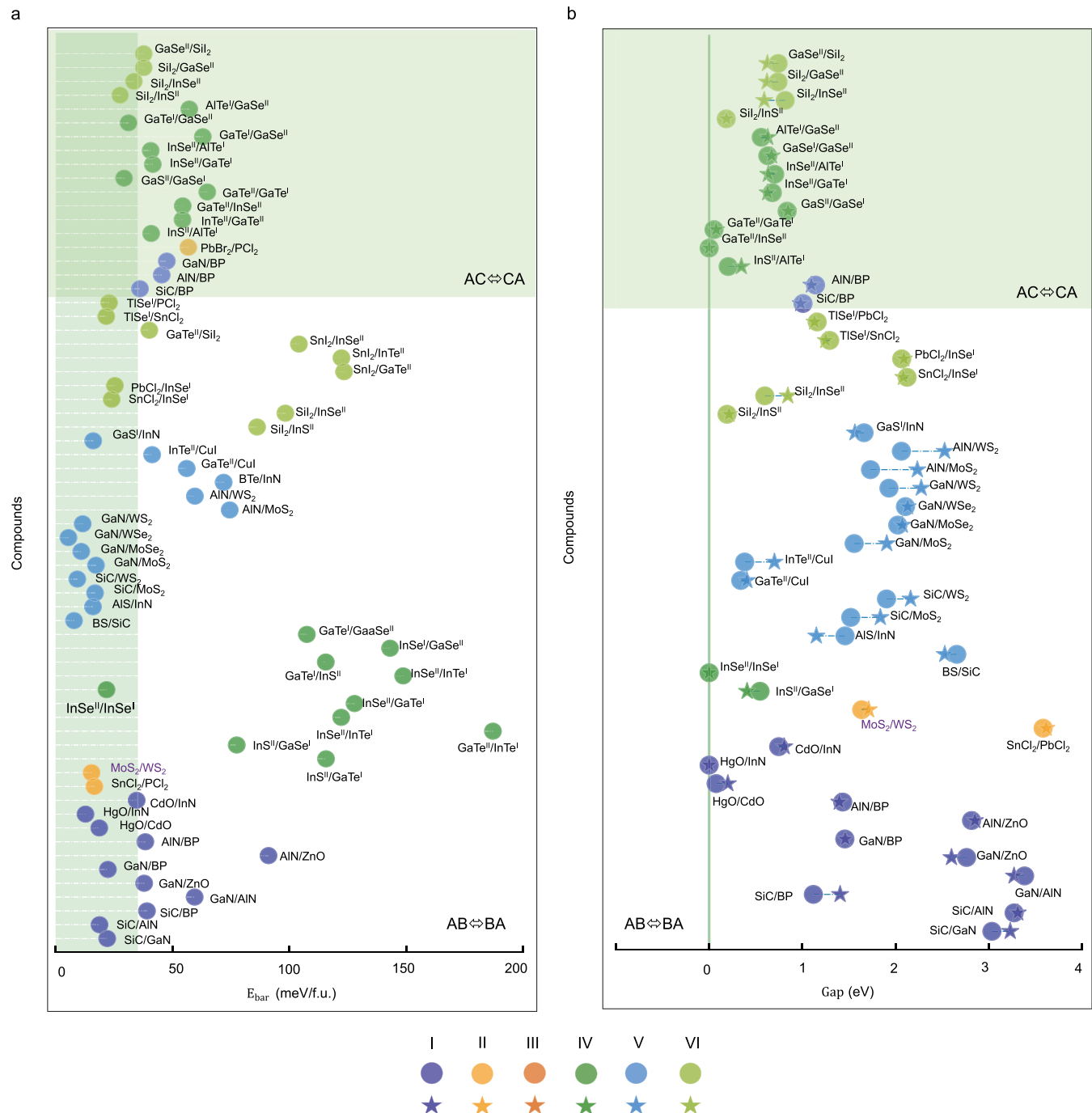


**Figure 5. Identification of low-barrier sliding ferroelectrics with optimal band gaps. (a)** The sliding energy barriers during sliding (less than 200 meV/f.u.) with an OOP larger than that of  $\text{MoS}_2/\text{WS}_2$  between AB and BA, AC and CA. **(b)** Band gaps of the same AB/BA and AC/CA stackings with sliding barriers below 100 meV/f.u.; circles represent AB and AC stackings; five-pointed stars denote BA and CA stacking.

referred to as decomposed method I (see Figure 1c), with their respective relationships to OOP variations between the two states clearly illustrated. For systems with the largest OOP variations, such as CdO/InN, the intra- and interlayer OOP contribute in the same direction. However, for most studied materials, their intra- and interlayer OOP contributions oppose each other. This indicates that adjusting the relative strengths of intra- and interlayer OOP during sliding is a key factor influencing the OOP, which is largely determined by the atomic arrangement within the monolayer and the interlayer stacking patterns. For instance, among the stacking types during sliding,

type I and type III exhibit the most notable OOP variations, while other types show relatively minor changes. Type I is dominated by interlayer OOP, which contributes positively, as exemplified by CdO/InN, HgO/InN, AlN/ZnO, HgO/CdO, GaN/AlN, and GaN/ZnO. In contrast, for type III, their intralayer OOP dominate and contribute positively, as observed in  $\text{BiCl}_3/\text{PI}_3$ ,  $\text{AsI}_3/\text{PI}_3$ ,  $\text{AsBr}_3/\text{PI}_3$ , and  $\text{SbCl}_3/\text{PI}_3$ .

Furthermore, the contributions of each layer in the heterobilayer are traced. Figure 4b presents the decomposition of intralayer contributions from individual layers within the heterobilayer. For type I, the primary contributors include CdO,

InN, AlN, and GaN. For type III, notable contributions arise from  $\text{PI}_3$ ,  $\text{AsI}_3$ , and  $\text{SbCl}_3$ . Interestingly, in systems like  $\text{CdO}/\text{InN}$  and  $\text{HgO}/\text{InN}$ , InN exhibits a negative contribution, while CdO and HgO contribute positively. Conversely, both upper and lower layers generally contribute negatively in types II, IV, V, and VI. In type III systems, such as  $\text{AsI}_3/\text{PI}_3$  and  $\text{SbCl}_3/\text{PI}_3$ , both layers contribute positively. Figure 4c illustrates the decomposition of interlayer contributions by individual layers, considering only the charge-related effect due to their coordinate dependence in OOP. For type I, a strong positive correlation between charge transfer and OOP is observed, except in the cases of  $\text{CdO}/\text{InN}$  and  $\text{HgO}/\text{InN}$ , where intralayer contributions are either positive or near-zero. In contrast, for type III, no clear correlation is evident as intralayer dipoles dominate the OOP, and the impact of interlayer charge transfer is relatively minor.

The above analysis focuses on combinations of positive and negative ions within the upper or lower layers. Next, we trace how the interactions between the anionic and cationic groups of the upper and lower layers in the heterobilayer influence the variations in sliding FE. As illustrated in Figure 1c, decomposition method II considers combinations of positive-positive and negative-negative atomic groups, whereas decomposition method III examines cross positive-negative atomic group pairs between the upper and lower layers to elucidate charge separation during sliding. As shown in Figure 4d–g, notable changes in charge distribution are observed during sliding, with the most pronounced variations occurring in type III structures. Moreover, this analysis effectively demonstrates how manipulating atomic species influences the OOP strength. For instance, in  $\text{AlN}/\text{ZnO}$  and  $\text{GaN}/\text{ZnO}$ , fixed anions with varying cations alter OOP. Similarly, in  $\text{AsI}_3/\text{PI}_3$  and  $\text{AsBr}_3/\text{PI}_3$ , fixed cations with varying anions achieve similar effects. Additionally, simultaneous changes in both layers, such as in  $\text{CdO}/\text{InN}$  and  $\text{ZnO}/\text{AlN}$ , where fixed anions and varying cations are employed further demonstrate the impact of cation manipulation on the OOP.

Since each layer is composed of positive and negative ions or groups, the OOP is further decomposed into contributions from Group<sup>+</sup> and Group<sup>-</sup> atomic groups within the upper and lower layers. Figure 4h shows the localized contributions from each group. Group<sup>+</sup> dominates in most types I, II, IV, V, and VI structures, while Group<sup>-</sup> has the largest contribution in type III. Figure 4i highlights the nonlocal charge-transfer contributions, where Group<sup>+</sup> generally dominates across most types. However, in type III, Group<sup>-</sup> contributions are also significant, reflecting the overall charge-transfer dynamics. This indicates that anions have a more pronounced impact on the OOP for type III, whereas cations play a more dominant role in other types. These findings reveal the underlying mechanisms driving OOP changes in the opposition in various types of monolayer materials when stacked into heterobilayers, providing valuable guidance for designing high-performance sliding ferroelectric materials with enhanced OOP.

**Sliding Energy Barriers and Band Gap for Applications.** The practical application of sliding ferroelectric materials is predominantly influenced by two key factors: the switching energy barrier ( $E_{\text{bar}}$ ) and the band gap.<sup>22,23,40</sup> To address this, we systematically analyzed the heterobilayer systems with typical stacking patterns, including AB/BA and AC/CA, focusing on those with  $E_{\text{bar}} < 200 \text{ meV/f.u.}$  and OOP values surpassing those of  $\text{MoS}_2/\text{WS}_2$  (OOP = 0.21,  $-0.78 \text{ pC/m}$  and  $E_{\text{bar}} = 15.3 \text{ meV/f.u.}$ ), as shown in Figure 5a and Table S4. Among the analyzed

heterobilayer systems, 40 materials exhibit OOP values surpassing those of  $\text{MoS}_2/\text{WS}_2$  while maintaining switching energy barriers below 50 meV/f.u., indicating their robust sliding ferroelectric performance and energy-efficient switching pathways. Compared to other reported intrinsic 2D ferroelectric materials with barriers reaching up to 76 meV/f.u.<sup>41</sup> and bulk materials with barriers as high as 380 meV/f.u.,<sup>42</sup> these heterobilayers demonstrate significantly lower sliding switching barriers. Considering the experimentally reported sliding energy barrier of 30 meV/f.u. for yttrium-doped  $\gamma\text{-InSe}$ ,<sup>43</sup> these heterobilayers demonstrate strong potential for experimental synthesis and practical applications. Additionally, 21 materials exhibit low-energy barriers (<35 meV/f.u.), indicating high potential for energy-efficient and low-cost polarization switching. Representative examples include  $\text{CdO}/\text{InN}$  ( $-8.94, 11.18 \text{ pC/m}$ , and  $34.6 \text{ meV/f.u.}$ ),  $\text{HgO}/\text{InN}$  ( $-8.34, 11.28 \text{ pC/m}$ , and  $12.7 \text{ meV/f.u.}$ ), and  $\text{SiC}_2/\text{WS}_2$  ( $-1.77, 1.04 \text{ pC/m}$ , and  $9.2 \text{ meV/f.u.}$ ). Moreover, these heterobilayers achieve OOP values exceeding those of  $\text{MoS}_2/\text{WS}_2$  while maintaining much lower energy barriers, making them highly promising candidates for experimental realization and practical applications.

Sliding FE materials exhibit the capability to reverse ferroelectric polarization through interlayer sliding. However, the presence of an appropriate band gap is crucial for achieving energy-efficient operation and compatibility with current Si-based technologies.<sup>44,45</sup> Using the HSE06 method, we calculated the band gaps of heterostructures with AB/BA and AC/CA stackings, where the OOP exceeds that of  $\text{MoS}_2/\text{WS}_2$  and the energy barrier is less than 100 meV/f.u., as shown in Figure 5b. Semiconducting properties are exhibited in 43 materials, making them highly suitable for sliding ferroelectric applications. Notable examples include heterobilayers with band gaps ranging from 0.7 to 3.5 eV, featuring sliding FE and low-energy barriers. Representative systems include  $\text{CdO}/\text{InN}$ ,  $\text{GaN}/\text{ZnO}$ ,  $\text{SiC}/\text{AlN}$ ,  $\text{SiC}/\text{GaN}$ ,  $\text{SiC}_2/\text{WS}_2$ ,  $\text{GaN}/\text{MoSe}_2$ ,  $\text{GaN}/\text{WSe}_2$ , and  $\text{GaN}/\text{WS}_2$ . In contrast, a few materials, such as  $\text{HgO}/\text{InN}$ ,  $\text{InSe}^{\text{I}}/\text{InSe}^{\text{II}}$ , and  $\text{GaTe}^{\text{II}}/\text{InSe}^{\text{II}}$ , display metallic behavior, which renders them unsuitable for practical sliding FE applications due to the absence of a band gap. Although  $\text{HgO}/\text{InN}$  exhibits the highest OOP ( $-8.34$  and  $11.28 \text{ pC/m}$ ) and a low sliding barrier ( $12.7 \text{ meV/f.u.}$ ), the metallic nature limits its applicability in sliding ferroelectric devices. Nevertheless, our study provides alternative candidate materials with a large OOP and tunable band gaps for practical implementation.

The predicted sliding ferroelectric heterobilayers exhibit a compelling combination of switchable OOP, moderate energy barriers, and semiconducting behavior—essential for practical device applications.<sup>18,22,23,46,47</sup> Their atomically thin geometry and electrically tunable interlayer polarization render them especially suitable for integration into nonvolatile ferroelectric memories, reconfigurable logic circuits, and neuromorphic computing architectures.<sup>4,48–50</sup> The intrinsic layered structure allows for controlled stacking and facilitates integration with existing semiconductor platforms, while their mechanical flexibility and chemical tunability further expand their potential for use in wearable and flexible electronics.<sup>51–53</sup> In addition to proposing guiding principles for designing high-performance sliding ferroelectrics, recent theoretical advances have unveiled alternative switching mechanisms involving the superlubric motion of domain walls (DWs).<sup>54–56</sup> Governed by symmetry breaking and the tensorial nature of Born effective charges (BECs), this ferrottribological pathway enables electric-field-induced polarization reversal without requiring large-scale

structural displacement, offering a promising route toward energy-efficient, fatigue-resistant, and deterministic operation—particularly suited for cryogenic logic and adaptive computing.<sup>54</sup> Together with the favorable electronic and mechanical attributes identified in our study, these emerging insights establish sliding ferroelectric heterobilayers as versatile and forward-looking platforms for next-generation nanoelectronic and multifunctional technologies.

## CONCLUSIONS

Overall, our high-throughput screening yields a comprehensive library of previously unreported sliding ferroelectrics. Among them, CdO/InN exhibits an OOP nearly 50 times greater than that of MoS<sub>2</sub>/WS<sub>2</sub>, coupled with a low sliding barrier, making it a system that simultaneously achieves strong polarization and energy-efficient switching. Beyond material identification, our study uncovers a fundamental structure–property relationship that governs sliding FE in 2D heterobilayers. By resolving polarization contributions across atomic, group, and layer levels, we reveal that the competition between inter- and intralayer dipoles plays a decisive role in stabilizing switchable OOP. This mechanistic insight explains why heterobilayers composed of single-atom-layer monolayers consistently yield optimal ferroelectric performance. In addition to expanding the accessible material space, our framework provides a predictive and physically interpretable pathway for engineering low-barrier, high-polarization systems, offering alternative opportunities for the rational design of 2D ferroelectrics in future memory and logic technologies.

## METHODS

All first-principles calculations were conducted using the Vienna Ab Initio Simulation Package (VASP) within the framework of density functional theory (DFT).<sup>57,58</sup> The projector-augmented wave (PAW) method was employed to accurately describe the interactions between core and valence electrons.<sup>59</sup> The exchange–correlation functional was treated using the Perdew–Burke–Ernzerhof (PBE) formulation within the generalized gradient approximation (GGA).<sup>60</sup> A plane-wave basis set with an energy cutoff of 600 eV was chosen to ensure the convergence of the total energies. Electronic minimization was performed with a strict convergence threshold of 10<sup>−6</sup> eV. Atomic structures were relaxed with a force convergence criterion of 0.005 eV/Å. To eliminate spurious interactions between periodically repeated units, a vacuum layer of at least 20 Å was introduced along the out-of-plane direction. The Brillouin zone was sampled using a Γ-centered 15 × 15 × 1 Monkhorst–Pack *k*-point mesh,<sup>61</sup> ensuring sufficient accuracy in the evaluation of electronic and structural properties. Considering the importance of vdW interactions in layered materials, the D3 Grimme correction<sup>62</sup> was adopted to capture the dispersive forces between layers accurately. The Berry phase method with dipole corrections was applied to calculate the out-of-plane ferroelectric polarization, with the corrections mitigating artifacts associated with periodic boundary conditions.<sup>63,64</sup> The PBE-D3 method was validated against reported sliding ferroelectrics.<sup>18,19,24,26</sup> As shown in Figure S5, the PBE-D3 method with dipole correction was used for OOP calculations. The energy barriers associated with polarization switching and interlayer sliding were evaluated using the climbing image nudged elastic band (CI-NEB) method.<sup>65</sup> The electronic structure was evaluated using the HSE06 hybrid functional, which is known to provide reliable predictions of band gaps in semiconductors.<sup>66</sup>

## ASSOCIATED CONTENT

### Supporting Information

The Supporting Information is available free of charge at <https://pubs.acs.org/doi/10.1021/acsnano.Sc11217>.

Computational analysis of OOP in bilayer stacking configurations; this includes definitions of stacking types and effective van der Waals distance, computed OOP values, and polarization switching barriers (below 100 meV/f.u.); and correlations with electronegativity differences and the decomposition of OOP into inter- and intra-atomic contributions are provided ([PDF](#))

## AUTHOR INFORMATION

### Corresponding Authors

Lei Shen – Department of Mechanical Engineering, National University of Singapore, Singapore 117575, Singapore; [orcid.org/0000-0001-6198-5753](https://orcid.org/0000-0001-6198-5753); Email: [shenlei@nus.edu.sg](mailto:shenlei@nus.edu.sg)

Yuan Ping Feng – Department of Physics, National University of Singapore, Singapore 117551, Singapore; [orcid.org/0000-0003-2190-2284](https://orcid.org/0000-0003-2190-2284); Email: [phyfyp@nus.edu.sg](mailto:phyfyp@nus.edu.sg)

### Authors

Xian Wang – Department of Physics, National University of Singapore, Singapore 117551, Singapore; School of Chemistry, Chemical Engineering and Biotechnology, Nanyang Technological University, 637371, Singapore; [orcid.org/0000-0002-4017-8036](https://orcid.org/0000-0002-4017-8036)

Jun Zhou – Institute of Materials Research and Engineering (IMRE), Agency for Science, Technology and Research (A\*STAR), Singapore 138634, Singapore; [orcid.org/0000-0002-5505-7616](https://orcid.org/0000-0002-5505-7616)

Xuesen Wang – Department of Physics, National University of Singapore, Singapore 117551, Singapore

Complete contact information is available at:  
<https://pubs.acs.org/10.1021/acsnano.Sc11217>

### Author Contributions

X.W., L.S., and Y.P.F. conceived the idea and designed the simulations. X.W. conducted the DFT calculations and performed the theoretical analysis. X.W. prepared the initial draft of the manuscript. Y.P.F. and L.S. supervised the project. The results were thoroughly discussed and analyzed by X.W., Y.P.F., L.S., J.Z., and X.S.W., contributing to the final interpretation of the findings.

### Notes

The authors declare no competing financial interest.

## ACKNOWLEDGMENTS

Y.P.F. and X.W. acknowledge Singapore MOE Tier 2 (No. MOE2019-T2-2-030). L.S. acknowledges the financial support from Singapore MOE Tier 1 (No. A-8001194-00-00) and Singapore MOE Tier 2 (No. A-8001872-00-00). L.S. and X.S.W. acknowledge the financial support from Singapore MOE Tier 1 (No. 23-0450-A0001).

## REFERENCES

- (1) Martin, L. W.; Rappe, A. M. Thin-film ferroelectric materials and their applications. *Nat. Rev. Mater.* **2017**, 2, No. 16087.
- (2) Jia, X.; Guo, R.; Tay, B. K.; Yan, X. Flexible ferroelectric devices: status and applications. *Adv. Funct. Mater.* **2022**, 32, No. 2205933.
- (3) Scott, J. F. Applications of Modern Ferroelectrics. *Science* **2007**, 315, 954–959.
- (4) Yasuda, K.; Zalys-Geller, E.; Wang, X.; Bennett, D.; Cheema, S. S.; Watanabe, K.; Taniguchi, T.; Kaxiras, E.; Jarillo-Herrero, P.; Ashoori, R. Ultrafast high-endurance memory based on sliding ferroelectrics. *Science* **2024**, 385, 53–56.

- (5) Bian, R.; Cao, G.; Pan, E.; Liu, Q.; Li, Z.; Liang, L.; Wu, Q.; Ang, L. K.; Li, W.; Zhao, X.; Liu, F. High-performance sliding ferroelectric transistor based on Schottky barrier tuning. *Nano Lett.* **2023**, *23*, 4595–4601.
- (6) Junquera, J.; Ghosez, P. Critical thickness for ferroelectricity in perovskite ultrathin films. *Nature* **2003**, *422*, 506–509.
- (7) Choi, K. J.; Biegalski, M.; Li, Y.; Sharan, A.; Schubert, J.; Uecker, R.; Reiche, P.; Chen, Y.; Pan, X.; Gopalan, V.; et al. Enhancement of ferroelectricity in strained BaTiO<sub>3</sub> thin films. *Science* **2004**, *306*, 1005–1009.
- (8) Ramesh, R.; Spaldin, N. A. Multiferroics: progress and prospects in thin films. *Nat. Mater.* **2007**, *6*, 21–29.
- (9) Deb, S.; Cao, W.; Raab, N.; Watanabe, K.; Taniguchi, T.; Goldstein, M.; Kronik, L.; Urbakh, M.; Hod, O.; Shalom, M. B. Cumulative polarization in conductive interfacial ferroelectrics. *Nature* **2022**, *612*, 465–469.
- (10) Man, P.; Huang, L.; Zhao, J.; Ly, T. H. Ferroic phases in two-dimensional materials. *Chem. Rev.* **2023**, *123*, 10990–11046.
- (11) Li, T.; Wu, Y.; Yu, G.; Li, S.; Ren, Y.; Liu, Y.; Liu, J.; Feng, H.; Deng, Y.; Chen, M.; et al. Realization of sextuple polarization states and interstate switching in antiferroelectric CuInP<sub>2</sub>S<sub>6</sub>. *Nat. Commun.* **2024**, *15*, No. 2653.
- (12) Zhang, D.; Schoenherr, P.; Sharma, P.; Seidel, J. Ferroelectric order in van der Waals layered materials. *Nat. Rev. Mater.* **2023**, *8*, 25–40.
- (13) Akamatsu, T.; Ideue, T.; Zhou, L.; Dong, Y.; Kitamura, S.; Yoshii, M.; Yang, D.; Onga, M.; Nakagawa, Y.; Watanabe, K.; et al. A van der Waals interface that creates in-plane polarization and a spontaneous photovoltaic effect. *Science* **2021**, *372*, 68–72.
- (14) Kruse, M.; Petralanda, U.; Gjerding, M. N.; Jacobsen, K. W.; Thygesen, K. S.; Olsen, T. Two-dimensional ferroelectrics from high throughput computational screening. *npj Comput. Mater.* **2023**, *9*, No. 45.
- (15) Wu, Y.; Abdelwahab, I.; Kwon, K. C.; Verzhbitskiy, I.; Wang, L.; Liew, W. H.; Yao, K.; Eda, G.; Loh, K. P.; Shen, L.; Quek, S. Y. Data-driven discovery of high performance layered van der Waals piezoelectric NbOI<sub>2</sub>. *Nat. Commun.* **2022**, *13*, No. 1884.
- (16) Chang, K.; Liu, J.; Lin, H.; Wang, N.; Zhao, K.; Zhang, A.; Jin, F.; Zhong, Y.; Hu, X.; Duan, W.; et al. Discovery of robust in-plane ferroelectricity in atomic-thick SnTe. *Science* **2016**, *353*, 274–278.
- (17) Zhou, J.; Shen, L.; Costa, M. D.; Persson, K. A.; Ong, S. P.; Huck, P.; Lu, Y.; Ma, X.; Chen, Y.; Tang, H.; Feng, Y. P. 2DMatPedia, an open computational database of two-dimensional materials from top-down and bottom-up approaches. *Sci. Data* **2019**, *6*, No. 86.
- (18) Li, L.; Wu, M. Binary compound bilayer and multilayer with vertical polarizations: two-dimensional ferroelectrics, multiferroics, and nanogenerators. *ACS Nano* **2017**, *11*, 6382–6388.
- (19) Yasuda, K.; Wang, X.; Watanabe, K.; Taniguchi, T.; Jarillo-Herrero, P. Stacking-engineered ferroelectricity in bilayer boron nitride. *Science* **2021**, *372*, 1458–1462.
- (20) Stern, M. V.; Waschitz, Y.; Cao, W.; Nevo, I.; Watanabe, K.; Taniguchi, T.; Sela, E.; Urbakh, M.; Hod, O.; Shalom, M. B. Interfacial ferroelectricity by van der Waals sliding. *Science* **2021**, *372*, 1462–1466.
- (21) Meng, P.; Wu, Y.; Bian, R.; Pan, E.; Dong, B.; Zhao, X.; Chen, J.; Wu, L.; Sun, Y.; Fu, Q.; et al. Sliding induced multiple polarization states in two-dimensional ferroelectrics. *Nat. Commun.* **2022**, *13*, No. 7696.
- (22) Wu, M. Two-dimensional van der Waals ferroelectrics: scientific and technological opportunities. *ACS Nano* **2021**, *15*, 9229–9237.
- (23) Wu, M.; Li, J. Sliding ferroelectricity in 2D van der Waals materials: Related physics and future opportunities. *Proc. Natl. Acad. Sci. U.S.A.* **2021**, *118*, No. e2115703118.
- (24) Wang, Z.; Gui, Z.; Huang, L. Sliding ferroelectricity in bilayer honeycomb structures: A first-principles study. *Phys. Rev. B* **2023**, *107*, No. 035426.
- (25) Liu, X.; Pyatakov, A. P.; Ren, W. Magnetoelectric coupling in multiferroic bilayer VS<sub>2</sub>. *Phys. Rev. Lett.* **2020**, *125*, No. 247601.
- (26) Wang, X.; Yasuda, K.; Zhang, Y.; Liu, S.; Watanabe, K.; Taniguchi, T.; Hone, J.; Fu, L.; Jarillo-Herrero, P. Interfacial ferroelectricity in rhombohedral-stacked bilayer transition metal dichalcogenides. *Nat. Nanotechnol.* **2022**, *17*, 367–371.
- (27) Fei, Z.; Zhao, W.; Palomaki, T. A.; Sun, B.; Miller, M. K.; Zhao, Z.; Yan, J.; Xu, X.; Cobden, D. H. Ferroelectric switching of a two-dimensional metal. *Nature* **2018**, *560*, 336–339.
- (28) Hou, W.; Azizimanesh, A.; Sewaket, A.; Peña, T.; Watson, C.; Liu, M.; Askari, H.; Wu, S. M. Strain-based room-temperature non-volatile MoTe<sub>2</sub> ferroelectric phase change transistor. *Nat. Nanotechnol.* **2019**, *14*, 668–673.
- (29) Wang, X.; Li, Y.; Zhang, Y.; Wang, P.; Zhao, Y.-M.; Zhou, J.; Yang, J.; Wang, X.; Shen, L. Machine learning assisted identification of homobilayer sliding ferroelectrics with large out-of-plane polarization and low sliding energy barriers. *Phys. Rev. B* **2025**, *111*, No. 094106.
- (30) Novoselov, K. S.; Mishchenko, A.; Carvalho, A.; Neto, A. H. C. 2D materials and van der Waals heterostructures. *Science* **2016**, *353*, No. aac9439.
- (31) Castellanos-Gomez, A.; Duan, X.; Fei, Z.; Gutierrez, H. R.; Huang, Y.; Huang, X.; Quereda, J.; Qian, Q.; Sutter, E.; Sutter, P. Van der Waals heterostructures. *Nat. Rev. Methods Primers* **2022**, *2*, No. 58.
- (32) Tran, K.; Moody, G.; Wu, F.; Lu, X.; Choi, J.; Kim, K.; Rai, A.; Sanchez, D. A.; Quan, J.; Singh, A.; et al. Evidence for moiré excitons in van der Waals heterostructures. *Nature* **2019**, *567*, 71–75.
- (33) Rivera, P.; Yu, H.; Seyler, K. L.; Wilson, N. P.; Yao, W.; Xu, X. Interlayer valley excitons in heterobilayers of transition metal dichalcogenides. *Nat. Nanotechnol.* **2018**, *13*, 1004–1015.
- (34) Xu, D.; Zhang, Q.; Huo, X.; Wang, Y.; Yang, M. Advances in data-assisted high-throughput computations for material design. *Mater. Genome Eng. Adv.* **2023**, *1*, No. e11.
- (35) Wang, X.; Wang, P.; Liu, X.; Wang, X.; Lu, Y.; Shen, L. Data-Driven Discovery of High-Performance Heterobilayer Transition Metal Dichalcogenide-Based Sliding Ferroelectrics. *ACS Appl. Mater. Interfaces* **2025**, *17*, 7164–7173.
- (36) Rogée, L.; Wang, L.; Zhang, Y.; Cai, S.; Wang, P.; Chhowalla, M.; Ji, W.; Lau, S. P. Ferroelectricity in untwisted heterobilayers of transition metal dichalcogenides. *Science* **2022**, *376*, 973–978.
- (37) Fu, J.; Kuksma, M.; Larsen, A. H.; Shinohara, K.; Togo, A.; Thygesen, K. S. Symmetry classification of 2D materials: layer groups versus space groups. *2D Mater.* **2024**, *11*, No. 035009.
- (38) Yang, Q.; Wu, M.; Li, J. Origin of two-dimensional vertical ferroelectricity in WTe<sub>2</sub> bilayer and multilayer. *J. Phys. Chem. Lett.* **2018**, *9*, 7160–7164.
- (39) Hirshfeld, F. L. Bonded-atom fragments for describing molecular charge densities. *Theor. Chim. Acta* **1977**, *44*, 129–138.
- (40) Fox, C.; Mao, Y.; Zhang, X.; Wang, Y.; Xiao, J. Stacking order engineering of two-dimensional materials and device applications. *Chem. Rev.* **2024**, *124*, 1862–1898.
- (41) Cheng, X.; Xu, S.; Liu, C.; Cui, Y.; Ouyang, W.; Jia, F.; Wu, W.; Ren, W. Ferroelectric and negative piezoelectric properties in oxyhydroxide monolayers  $\gamma$ -XOOH (X = Al, Ga, and In). *Appl. Phys. Lett.* **2023**, *123*, No. 072904.
- (42) Gao, W.; Chelikowsky, J. R. Prediction of intrinsic ferroelectricity and large piezoelectricity in monolayer arsenic chalcogenides. *Nano Lett.* **2020**, *20*, 8346–8352.
- (43) Sui, F.; Li, H.; Qi, R.; Jin, M.; Lv, Z.; Wu, M.; Liu, X.; Zheng, Y.; Liu, B.; Ge, R.; et al. Atomic-level polarization reversal in sliding ferroelectric semiconductors. *Nat. Commun.* **2024**, *15*, No. 3799.
- (44) Hadke, S.; Kang, M.-A.; Sangwan, V. K.; Hersam, M. C. Two-Dimensional Materials for Brain-Inspired Computing Hardware. *Chem. Rev.* **2025**, *125*, 835–932.
- (45) Zhao, Y.; Gobbi, M.; Hueso, L. E.; Samori, P. Molecular approach to engineer two-dimensional devices for CMOS and beyond-CMOS applications. *Chem. Rev.* **2022**, *122*, 50–131.
- (46) Li, T.; Deng, S.; Liu, H.; Chen, J. Insights into strain engineering: from ferroelectrics to related functional materials and beyond. *Chem. Rev.* **2024**, *124*, 7045–7105.
- (47) Zhang, Y.; Jie, W.; Chen, P.; Liu, W.; Hao, J. Ferroelectric and piezoelectric effects on the optical process in advanced materials and devices. *Adv. Mater.* **2018**, *30*, No. 1707007.

- (48) Bian, R.; He, R.; Pan, E.; Li, Z.; Cao, G.; Meng, P.; Chen, J.; Liu, Q.; Zhong, Z.; Li, W.; Liu, F. Developing fatigue-resistant ferroelectrics using interlayer sliding switching. *Science* **2024**, *385*, 57–62.
- (49) Duan, X.; Wang, C.; Pan, A.; Yu, R.; Duan, X. Two-dimensional transition metal dichalcogenides as atomically thin semiconductors: opportunities and challenges. *Chem. Soc. Rev.* **2015**, *44*, 8859–8876.
- (50) Zhang, L.; Dong, J.; Ding, F. Strategies, status, and challenges in wafer scale single crystalline two-dimensional materials synthesis. *Chem. Rev.* **2021**, *121*, 6321–6372.
- (51) Li, J.; Yang, X.; Zhang, Z.; Yang, W.; Duan, X.; Duan, X. Towards the scalable synthesis of two-dimensional heterostructures and superlattices beyond exfoliation and restacking. *Nat. Mater.* **2024**, *23*, 1326–1338.
- (52) Wilson, N. P.; Yao, W.; Shan, J.; Xu, X. Excitons and emergent quantum phenomena in stacked 2D semiconductors. *Nature* **2021**, *599*, 383–392.
- (53) Xue, G.; Qin, B.; Ma, C.; Yin, P.; Liu, C.; Liu, K. Large-area epitaxial growth of transition metal dichalcogenides. *Chem. Rev.* **2024**, *124*, 9785–9865.
- (54) Ke, C.; Liu, F.; Liu, S. Superlubric Motion of Wavelike Domain Walls in Sliding Ferroelectrics. *Phys. Rev. Lett.* **2025**, *135*, No. 046201.
- (55) Wang, Z.; Dong, S. Polarization switching in sliding ferroelectrics: Roles of fluctuation and domain wall. *Phys. Rev. B* **2025**, *111*, No. L201406.
- (56) Shi, Y.; Gao, Y.; Wang, H.; Zhang, B.; Zhong, Z.; He, R. Soliton-like domain wall motion in sliding ferroelectrics with ultralow damping. *Phys. Rev. B* **2025**, *112*, No. 035421.
- (57) Kresse, G.; Furthmüller, J. Efficiency of ab-initio total energy calculations for metals and semiconductors using a plane-wave basis set. *Comput. Mater. Sci.* **1996**, *6*, 15–50.
- (58) Kresse, G.; Furthmüller, J. Efficient iterative schemes for ab initio total-energy calculations using a plane-wave basis set. *Phys. Rev. B* **1996**, *54*, No. 11169.
- (59) Blöchl, P. E. Projector augmented-wave method. *Phys. Rev. B* **1994**, *50*, No. 17953.
- (60) Perdew, J. P.; Burke, K.; Ernzerhof, M. Generalized gradient approximation made simple. *Phys. Rev. Lett.* **1996**, *77*, No. 3865.
- (61) Monkhorst, H. J.; Pack, J. D. Special points for Brillouin-zone integrations. *Phys. Rev. B* **1976**, *13*, No. 5188.
- (62) Grimme, S.; Ehrlich, S.; Goerigk, L. Effect of the damping function in dispersion corrected density functional theory. *J. Comput. Chem.* **2011**, *32*, 1456–1465.
- (63) King-Smith, R. D.; Vanderbilt, D. Theory of polarization of crystalline solids. *Phys. Rev. B* **1993**, *47*, No. 1651.
- (64) Neugebauer, J.; Scheffler, M. Adsorbate-substrate and adsorbate-adsorbate interactions of Na and K adlayers on Al (111). *Phys. Rev. B* **1992**, *46*, No. 16067.
- (65) Henkelman, G.; Uberuaga, B. P.; Jónsson, H. A climbing image nudged elastic band method for finding saddle points and minimum energy paths. *J. Chem. Phys.* **2000**, *113*, 9901–9904.
- (66) Paier, J.; Marsman, M.; Hummer, K.; Kresse, G.; Gerber, I. C.; Ángyán, J. G. Screened hybrid density functionals applied to solids. *J. Chem. Phys.* **2006**, *124*, No. 154709.

CAS BIOFINDER DISCOVERY PLATFORM™

**PRECISION DATA FOR FASTER DRUG DISCOVERY**

CAS BioFinder helps you identify targets, biomarkers, and pathways

**Unlock insights**

**CAS**   
A division of the American Chemical Society